

Design of a LYSO Crystal Electromagnetic Calorimeter for DarkSHINE Experiment*

Zhiyu Zhao,^{1,2,3,†} Qibin Liu,^{1,2,3,†} Jiyuan Chen,^{2,3,1} Jing Chen,^{2,3,1} Junfeng Chen,^{4,5} Xiang Chen,^{2,3} Changbo Fu,^{6,7} Jun Guo,^{2,3} Kim Siang Khaw,^{1,2,3} Liang Li,^{2,3} Shu Li,^{1,2,3,‡} Danning Liu,^{1,2,3} Kun Liu,^{1,2,3,§} Siyuan Song,^{2,3,1} Tong Sun,^{1,2,3} Jiannan Tang,^{2,3} Yufeng Wang,^{1,2,3} Zhen Wang,^{1,2,3} Weihao Wu,^{2,3} Haijun Yang,^{2,3,1,¶} Yuming Lin,^{1,2,3} Rui Yuan,^{1,2,3} Yulei Zhang,^{2,3} Yunlong Zhang,^{8,9} Baihong Zhou,^{1,2,3} Xuliang Zhu,^{1,2,3} and Yifan Zhu^{2,3,1}

¹*Tsung-Dao Lee Institute, Shanghai Jiao Tong University, 1 Lisuo Road, Shanghai 201210, China*

²*Institute of Nuclear and Particle Physics, School of Physics and Astronomy, 800 Dongchuan Road, Shanghai 200240, China*

³*Key Laboratory for Particle Astrophysics and Cosmology (MOE),*

Shanghai Key Laboratory for Particle Physics and Cosmology (SKLPPC),

Shanghai Jiao Tong University, 800 Dongchuan Road, Shanghai 200240, China

⁴*Center of Materials Science and Optoelectronics Engineering,*

University of Chinese Academy of Science, Beijing, 100049 China

⁵*Shanghai Institute of Ceramics, Chinese Academy of Sciences, Shanghai, 201899 China*

⁶*Key Laboratory of Nuclear Physics and Ion-beam Application (MOE), Fudan University, Shanghai, 200443, China*

⁷*Institute of Modern Physics, Fudan University, Shanghai, 200443, China*

⁸*State Key Laboratory of Particle Detection and Electronics,*

University of Science and Technology of China, Hefei 230026, China

⁹*Department of Modern Physics, University of Science and Technology of China, Hefei 230026, China*

This paper presents the design and optimization of a LYSO crystal-based electromagnetic calorimeter (ECAL) for the DarkSHINE experiment, which aims to search for dark photon as potential dark force mediator. The ECAL design has been meticulously evaluated through comprehensive simulations, focusing on optimizing dimensions, material choices, and placement within the detector array to enhance sensitivity in search for dark photon signatures while balancing cost and performance. The concluded ECAL design, comprising $2.5 \times 2.5 \times 4$ cm³ LYSO crystals arranged in a $52.5 \times 52.5 \times 44$ cm³ structure, ensures high energy resolution and effective energy containment. The study also explored the energy distribution across different ECAL regions and established a dynamic range for energy measurements, with a 4 GeV limit per crystal deemed sufficient. Additionally, the radiation tolerance of ECAL components was assessed, confirming the sustainability of LYSO crystals and radiation-resistant silicon sensors.

Keywords: Electromagnetic Calorimeter, LYSO, Scintillator Detector, Light Dark Matter, Dark Photon

I. INTRODUCTION

Dark matter (DM) [1, 2] remains one of the most compelling mysteries in cosmology and particle physics, evident from its gravitational effects on visible matter and the cosmic microwave background. The prevailing hypothesis is that DM, which does not interact with ordinary matters, constitutes about 85% of the universe's total mass. Understanding DM is crucial for unraveling the universe's structure and origins.

Theoretical models suggest that DM was produced through thermal processes in the early universe, with the "freeze-out" mechanism[3] explaining its current observed density, positing a probable mass range from a few MeV to several TeV. Despite extensive searches, the specific properties and particle nature of DM remain elusive. Experiments such as XENONnT[4], PandaX[5], CDEX[6], LUX-

ZEPLIN[7], AMS[8], DAMPE[9] and LHC[10] have narrowed the parameter space for weakly interacting massive particles (WIMPs)[11–17] in the GeV to TeV range, yet these particles remain undetected[18].

Given the high-mass DM candidate particles are yet to be detected, there is increasing interest in the sub-GeV mass range, which presents significant detection challenges due to the minimal interaction cross-sections of such light particles with ordinary matter. This has necessitated the development of innovative detection techniques distinct from traditional DM detection methods. Accelerator-based experiments are particularly promising, leveraging high-energy particle collisions to produce and detect dark photons, a hypothetical mediator between visible and dark matter[19–23]. Facilities such as CERN's NA64[24], LHC[25], BELLE-II[26], BES-III[27, 28], and the proposed LDMX[29] experiment aim to explore these possibilities.

The DarkSHINE experiment[31, 32], designed to operate under the minimal dark photon model, proposes a novel approach to detecting these elusive particles. Figure 1 illustrates the conceptual framework of dark photon production through dark bremsstrahlung and their subsequent decay into invisible dark matter, forming the experimental basis for DarkSHINE. This experiment leverages the high repetition rate electron beams provided by the Shanghai High Repetition-Rate XFEL and Extreme Light Facility (SHINE)[33, 34], optimized for detecting subtle signals that hint the presence of dark pho-

* This work was supported by National Key R&D Program of China (Grant No.: 2023YFA1606904 and 2023YFA1606900), National Natural Science Foundation of China (Grant No.: 12150006), and Shanghai Pilot Program for Basic Research—Shanghai Jiao Tong University (Grant No.: 21TQ1400209).

† These authors contributed equally to this work.

‡ Corresponding author, [Shu Li, shu.li@sjtu.edu.cn](mailto:Shu.Li@sjtu.edu.cn)

§ Corresponding author, [Kun Liu, kun.liu@sjtu.edu.cn](mailto:Kun.Liu@sjtu.edu.cn)

¶ Corresponding author, [Haijun Yang, haijun.yang@sjtu.edu.cn](mailto:Haijun.Yang@sjtu.edu.cn)

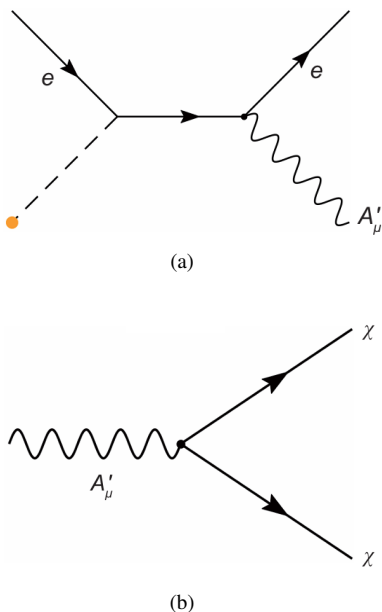


Fig. 1. Panel (a) Production of dark photons via bremsstrahlung. (b) Decay of dark photons into "invisible" modes, where the dark photon decays into dark matter particles that do not interact with ordinary matter. [30]

tons.

This paper delineates the design principles of the Electromagnetic Calorimeter (ECAL), focusing on the selection of materials and structural layout. Through comprehensive simulation studies, we have optimized the ECAL configuration, achieving a balance between performance and cost-efficiency. We also explored the dynamic range of energy that the ECAL's crystals can absorb. Insights from these analyses have guided the development of potential triggering strategies for future detectors. Additionally, we assessed the radiation tolerance of the ECAL, highlighting the necessity for crystals and silicon sensors that maintain high performance in high-radiation environments.

II. DARKSHINE EXPERIMENT AND ECAL DESIGN

DarkSHINE is a fixed-target experiment that focuses on the bremsstrahlung production of dark photons and measuring their invisible decay. It utilizes a high repetition rate single-electron beam provided by SHINE, which is currently under construction. The designed beam energy from SHINE is 8 GeV with a designed repetition rate of 1 MHz. The beam is expected to achieve an energy of 8 GeV and a repetition rate of 10 MHz. This corresponds to 3×10^{14} electron-on-target (EOT) events during one year of the DarkSHINE experiment's commissioning.

The primary challenge for DarkSHINE is to use information from various detectors to minimize background contributions while preserving the dark photon signal. Figure 2 shows the detector system of DarkSHINE. It primarily con-

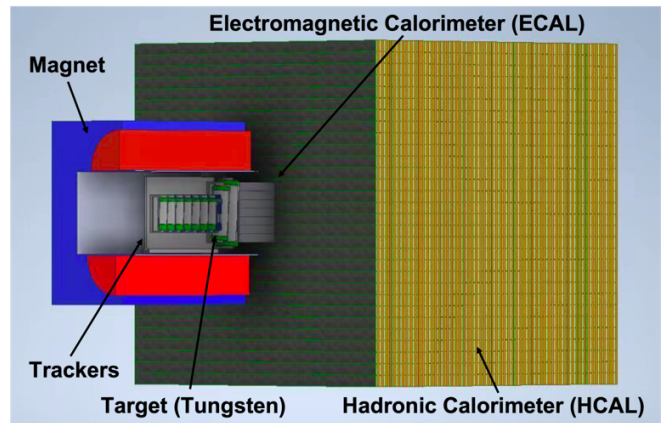


Fig. 2. Schematic of the DarkSHINE detector system, illustrating the primary components used for dark photon detection. The setup includes a tungsten target, a tagging tracker, a recoil tracker, an electromagnetic calorimeter (ECAL), and a hadronic calorimeter (HCAL)[31].

sists of a tungsten target ($0.1 X_0$) and three sub-detectors: a tracker, an electromagnetic calorimeter (ECAL), and a hadronic calorimeter (HCAL). Additionally, a single electron beam with a spatial distribution radius of 3 cm and a maximum non-uniform magnetic field of 1.5 Tesla in the tracker region were used in the simulations. The tracker measures the momentum and trajectory of electrons, consisting of a total of thirteen layers of silicon strips. Seven layers are placed in front of the target to tag the incident electron (tagging tracker), and six layers are placed behind the target (recoil tracker). A crystal ECAL positioned behind the recoil tracker measures the deposited energy of recoil electrons and photons. Then, a scintillator-steel based sampling HCAL is placed behind and surrounding the ECAL to capture and veto the backgrounds, in particular the neutral hadrons and muons.

To measure the invisible decay of dark photons, it is essential to precisely measure the energy of recoil electrons after each collision to determine if there is a significant energy loss. The core detector of DarkSHINE, the ECAL designed for DarkSHINE, is a homogeneous LYSO crystal calorimeter with very high electromagnetic energy resolution. LYSO[35–37] is an excellent choice for our crystal material, not only because of its high light yield, which is critical for electromagnetic resolution, but also due to its rapid scintillation decay time (40 ns), which is vital for handling the extremely high event rate we face. Furthermore, the ECAL, especially its central region, is exposed to a considerable radiation dose, necessitating materials with good radiation resistance. LYSO has shown exceptional durability in such conditions, establishing it as an optimal selection for DarkSHINE ECAL applications.

The radiation length of LYSO is about 1.12 cm. The transverse dimension of the ECAL is $52.5 \times 52.5 \text{ cm}^2$, with a dimension along the beam direction of 44 cm, approximately equivalent to 39 radiation lengths. The substantial depth ensures excellent energy containment in the ECAL, guaranteeing that it can absorb nearly all electromagnetic showers, pre-

venting them from leaking into the HCAL. This is crucial because such leakage would result in vetoing dark photon signals by the HCAL. The ECAL is fully segmented to gather comprehensive information, enhancing its capability to discriminate dark photons. After optimization, the ECAL is composed of $21 \times 21 \times 11$ LYSO crystals, with each crystal measuring $2.5 \times 2.5 \times 4 \text{ cm}^3$ and read out by SiPMs[38, 39]. In each layer, the crystals are positioned in a uniform 21×21 square pattern. To enhance detection efficacy and prevent particles from traversing the gaps, the placement of crystals in successive layers is shifted by half the transverse dimension of a crystal. This staggered structure aids in detecting recoil electron with energy loss coming along with dark photon signal.

III. SIMULATION, DIGITIZATION AND OPTIMIZATION

A. Simulation and digitization

1. Software setup

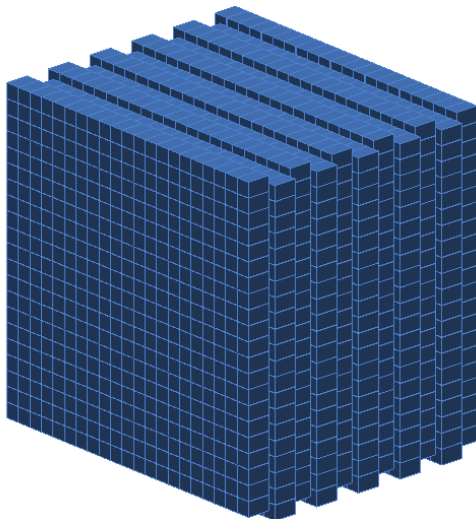


Fig. 3. Configuration of the Electromagnetic Calorimeter (ECAL) in DarkSHINE. The ECAL consists of an array of LYSO crystals, each coupled with SiPMs for readout. The schematic shows the segmentation and staggered layout of the crystals within the ECAL.

The Monte Carlo simulation of the ECAL is performed using the DarkSHINE Software (DSS) framework based on Geant4[40]. This simulation includes the entire detector setup, encompassing the crystal cubes, wrappers, SiPM sensors, and support structures, alongside other components like the Tracker and HCAL. This comprehensive setup provides the necessary reference for ECAL reconstruction and the initial analysis cuts to define the appropriate phase space for ECAL analysis. The detector configuration used in the simulation is illustrated in Figure 3. Within DSS, we can simulate inclusive events that include all background processes or individual simulations of dark photon processes and specific rare

background events.

The target is used in a "full simulation" scenario where an 8 GeV electron beam strikes the target as proposed in the experiment, and secondary particles traverse all detector components. In particular, an "ECAL-unit simulation" focuses on a single ECAL unit to study its precise effects, directly comparable with laboratory test results during R&D. All types of simulations are conducted with consistent material setups.

2. Energy Digitization

Accurate simulation of the response of crystal-based detectors requires a precise description of digitization effects. Digitization applies a series of realistic effects to the simulation results, mimicking the behavior of an actual detector and bringing the simulation more comparable to real experimental conditions. The energy directly obtained from Geant4, known as the truth energy, represents the ideal energy deposition of a particle in a perfect detection scenario, devoid of any detector effects or measurement errors. Thus, digitization provides a more realistic depiction of detector performance, offering stronger evidence for optimization.

The main goal of energy digitization is to parameterize the behavior of each element related to energy measurement. This involves applying smearing based on experimental data. For the DarkSHINE ECAL, the energy digitization process can be primarily divided into three parts: scintillation digitization, SiPM digitization, and ADC digitization.

Table 1. Parameters in scintillation digitization.

Scintillator	Light yield (intrinsic)	Light yield fluctuation
LYSO	30000 ph/MeV	10%
Light yield calibration accuracy	SiPM PDE (average)	Light yield (measured)
1%	6.3%	150 p.e./MeV

The first step is scintillation digitization. We set an intrinsic light yield of 30,000 photons per MeV for the LYSO crystal scintillator, assuming a 10% fluctuation across all scintillators. The scintillation light is proportional to the energy deposited in the crystal and follows a Poisson distribution. The scintillation light experiences attenuation during propagation within the crystal and detection by the SiPM. The attenuation depends on the photon transportation length and the detection efficiency of the SiPM. The measured light yield helps to determine the amount of light loss during propagation. Although the measured light yield for all crystal-SiPM units shows fluctuations, these can be calibrated to some extent, assumed here to have a 1% accuracy. The parameters used in this step are shown in Table 1.

For SiPM digitization, a toy Monte Carlo model simulates the SiPM's response to the scintillation light from the LYSO crystal. This simulation is based on the HAMAMATSU S14160-3010PS[41], featuring a $3 \times 3 \text{ mm}^2$ sensitive area, 10

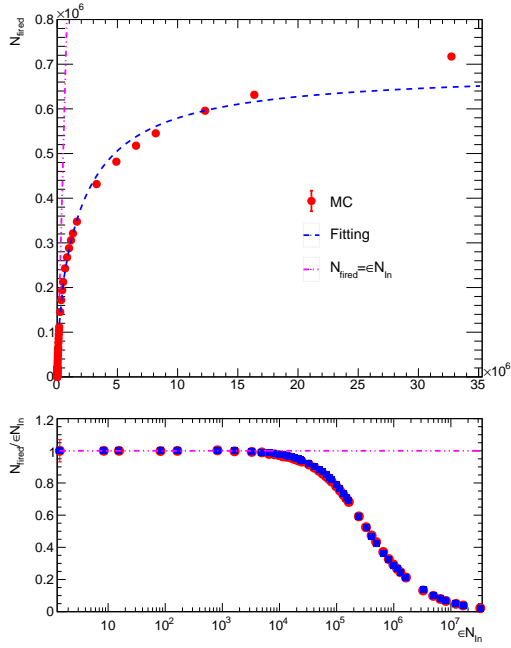


Fig. 4. Simulated SiPM response for HAMAMATSU S14160-3010PS, illustrating the relationship between the number of incident photons (N_{In}) and the number of fired pixels (N_{fired}). This simulation takes into account photon detection efficiency (PDE), pixel density, pixel recovery time, and crosstalk effects. The simulated points are fitted with a formula (blue dashed line), providing a description of the SiPM response and a method for correcting saturation effects.

Table 2. Parameters in SiPM digitization.

Pixel number	Crosstalk	Gain fluctuation	Gain calibration accuracy
89984	0.5%	10%	1%

μm pixels, and nearly 90,000 pixels in total. This model considers the photon detection efficiency, pixel density, pixel recovery, and crosstalk effect of the SiPM. Through this model, we can determine the SiPM's response to varying numbers of incident photons. As shown in Figure 4, N_{fired} is the number of photons detected by the SiPM, ϵ is the photon detection efficiency, and N_{In} is the number of photons incident on the SiPM. As the number of incident photons increases, the number of detected photons deviates from linearity and tends to saturate. A formula from [42] is used to fit the SiPM's response. This formula helps in simulating the SiPM's response to variable numbers of incident photons, providing a means to correct for saturation effects. Parameters in SiPM digitization are shown in Table 2.[43, 44]

The behavior of the readout electronics is simulated in the ADC digitization process. Here, we assume that the charge produced by the SiPM is recorded by a 12-bit multi-channel analyzer with a total of 4096 ADC channels. There are three gain modes to expand the dynamic range: high gain, medium gain, and low gain. In high gain and medium gain modes, when the ADC exceeds 4000, it will automatically switch to

Table 3. Parameters in ADC digitization.

Modes	Gain	ADC/p.e.	Noise
High gain	$\times 1$	10	3 ADC
Middle gain	$\times 45$	0.2	3 ADC
Low gain	$\times 2000$	0.005	3 ADC

Equivalent noise energy	Switching point	Energy range
2 keV	4000 ADC	10-2.7 MeV
100 keV	4000 ADC	2.7-133.3 MeV
4 MeV	-	133.3-5461 MeV

the next gain level. The smaller the gain, the larger the equivalent electronic noise. Table 3 shows the parameters used in ADC digitization.

In Tables 1, 2, and 3, some parameters are obtained based on a $2.5 \times 2.5 \times 4 \text{ cm}^3$ crystal, an optimized size discussed in section III C. Each part's contribution to the single-channel energy resolution is illustrated in Figure 5. We individually simulated the digitization process for each component to obtain its resolution and also simulated the process with all three components present to determine the overall resolution. At lower energies (less than 100 MeV), the resolution of the SiPM digitization is the main contributor. At higher energies, contributions from the scintillator digitization and ADC digitization become more significant.

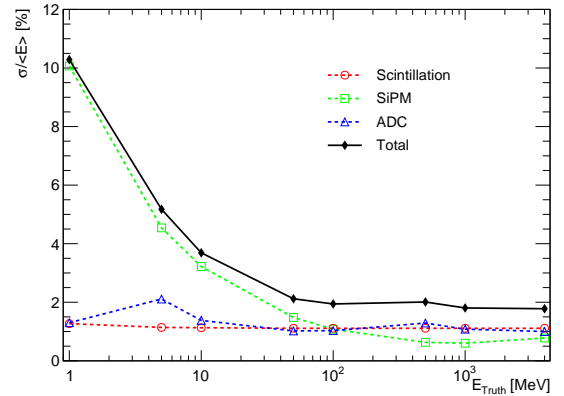
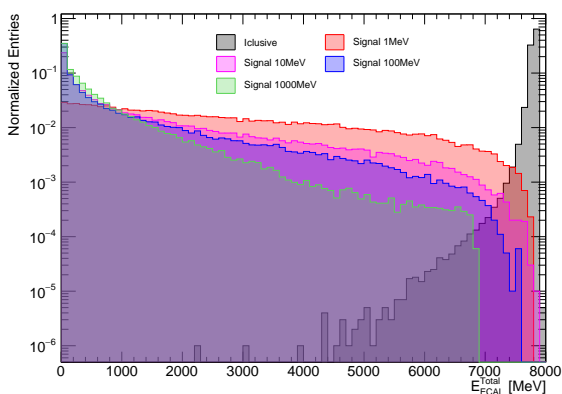


Fig. 5. Energy resolution of single channel for each digitization part and total effect. At energies below 100 MeV, the primary contributor to the resolution is the SiPM digitization. As the energy increases, the scintillator digitization and ADC digitization become the dominant factors.

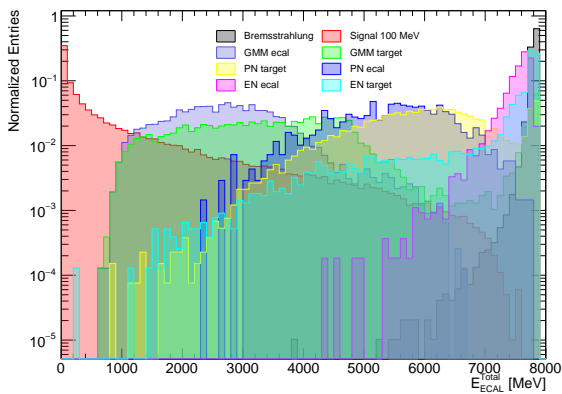
It should be noted that the current digitization is only used for the optimization of the crystal unit size in section III C. For other analyses involving the total ECAL energy, for simplicity, we only use the truth energy.

B. Signal and background

Signal and background processes exhibit distinct characteristics within different detectors. Typically, incident electrons pass through the target with negligible energy loss. In the tagging tracker and recoil tracker, each electron leaves a single track, and the measured momentum remains consistent across both trackers. Nearly all recoil electron energy is deposited in the electromagnetic calorimeter (ECAL), with minimal signals detected by the hadronic calorimeter (HCAL). In the ECAL, normal electron events usually show a significant energy deposition, typically around 8 GeV.



(a)



(b)

Fig. 6. Deposit energy in ECAL of different processes: (a) Dark photon and inclusive background processes. Inclusive background processes (grey) result in significantly higher energy deposition within the ECAL, reaching up to 8 GeV. In contrast, the energy deposition from dark photon signal processes is significantly lower, mainly concentrating around 0 GeV. (b) Dark photon and rare background processes. Only the bremsstrahlung process exhibits significantly distinct energy deposition in the ECAL compared to the signal, as its final state particles are electrons and photons. Other processes involving muons and nuclear reactions result in more energy deposition at the low-energy end and cannot be completely excluded by the ECAL.

When a dark photon is produced during the electron-on-target process, most of the incident energy transfers to it, and the recoiled electron deposits its remaining energy in the ECAL. The dark photon decays into dark matter, leaving no signal in the tracker or calorimeter, causing significant energy loss in the ECAL, typically exceeding 4 GeV (Figure 6). As the dark photon mass increases, it carries more energy from the electrons, leading to larger energy losses of the recoiled electron measured in the ECAL.

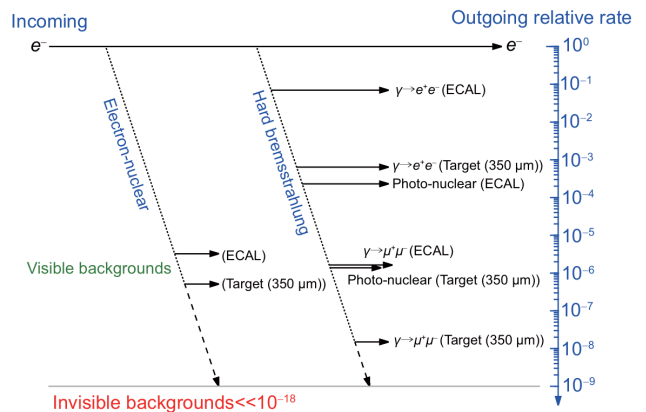


Fig. 7. Major background processes and their branching ratios in the DarkSHINE experiment. [31]

Figure 7 shows the major background processes and their relative rates. Background processes in the DarkSHINE experiment are categorized into two types: soft background, where the recoil electron loses less than 4 GeV, and hard background, where the energy loss exceeds 4 GeV.

Soft background processes, including normal electron events, dominate the total event production, constituting over 90%. These processes result in substantial energy deposition within the ECAL, making them easily distinguishable from dark photon signals.

In contrast, hard background processes remove most of the recoil electron's energy. If electrons undergo electromagnetic interactions, such as hard bremsstrahlung or conversion of bremsstrahlung photons into electron-positron pairs at the target, the energy deposited in the ECAL remains a critical rejection criterion. However, processes involving photon conversion into muon pairs are not easily distinguished by the ECAL and require exclusion by the HCAL and tracker. Background processes involving nuclear reactions, such as electron-nucleus interactions or bremsstrahlung photons interacting with nuclei, produce secondary particles with hadronic components, primarily neutrons[45]. These particles penetrate the ECAL and are to be vetoed by the HCAL or the tracker.

Neutrino-producing background processes, such as Moller scattering ($e^-e^- \rightarrow e^-e^-$) followed by a charged-current quasi-elastic (CCQE) reaction ($e^-p \rightarrow \nu_e n$), neutrino pair production ($e^-N \rightarrow e^-N\nu\nu$), bremsstrahlung with CCQE, and charge-current exchange with exclusive ($e^-p \rightarrow \nu n\pi^0$), as mentioned in [46], have been found negligible in this

experiment due to their low event ratios. Therefore, these backgrounds are currently excluded from the DarkSHINE simulation[31].

In summary, the ECAL effectively excludes all soft backgrounds and hard backgrounds that do not involve muons or hadrons.

C. Segmentation optimization

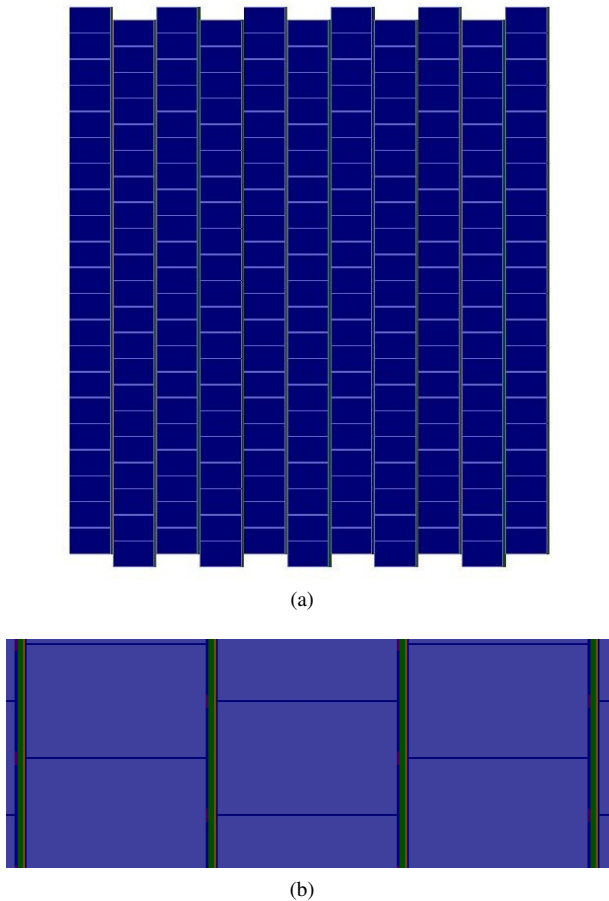


Fig. 8. (a) Structure of the ECAL viewed from the side. (b) Detailed structure of the ECAL for cell optimization, showing the placement of LYSO crystals (light blue), SiPMs (red), and the supporting PCB (green) and copper (gold) sheets used for electronic signal readout and cooling.

To thoroughly understand how crystal size influences energy measurement, a 1.2 mm thick PCB and a 0.5 mm thick copper plate were integrated behind each crystal layer for electronic signal readout and cooling purposes. Figure 8 depicts the detailed structure of the ECAL. Crystals are arranged in multiple layers along the beam direction, each layer consisting of uniformly positioned crystals. Each crystal is wrapped with an $80 \mu\text{m}$ ESR film and coupled with a 0.6 mm thick, $3 \times 3 \text{ mm}^2$ silicon piece at the end. A $20 \mu\text{m}$ air gap separates all materials. The ECAL comprises several thousand to tens of thousands of crystals, with the size affecting various

performance aspects, such as light collection efficiency and the amount of passive material introduced. This study optimizes the detector's performance by adjusting the crystal size to achieve high energy resolution and efficient energy containment.

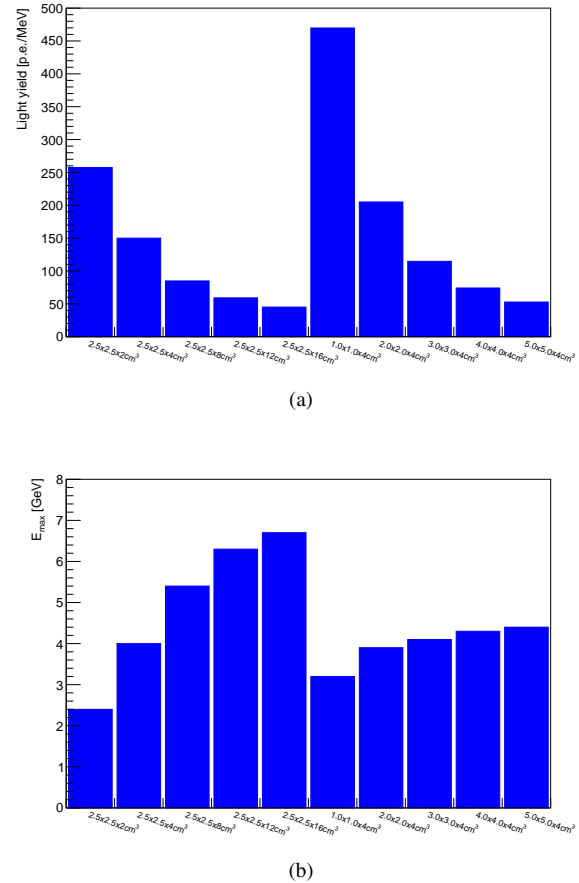
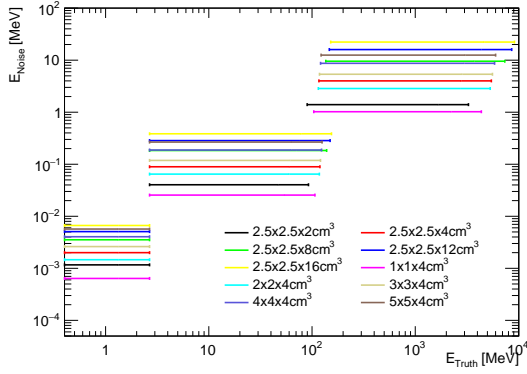


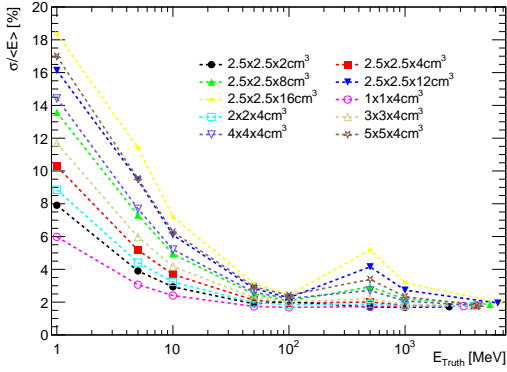
Fig. 9. (a) Light yield measured by SiPM from Geant4 optical simulation. (b) Maximum deposited energy within crystals under an 8 GeV electron beam incident on the ECAL. Crystals with smaller cross-sectional areas and shorter lengths exhibit higher light yields due to greater light collection efficiency, but this also results in lower energy absorption.

Figure 9 shows the simulated light yield and maximum deposited energy in LYSO crystals of various sizes. Crystals with smaller cross-sectional areas and shorter lengths exhibit higher light yields but lower deposited energy under an 8 GeV electron beam. The deposited energy was obtained from the full ECAL simulation. However, ECALs equipped with small crystals may contain more passive material due to the increased number of layers. Light yield and deposited energy influence the light output and the dynamic range of the electronics, while the amount of passive material impacts energy containment. These effects are quantified using the digitization tool.

Figure 10 illustrates the Equivalent Noise Energy (ENE) for crystals of different sizes. The ENE is calculated using



(a)



(b)

Fig. 10. (a) Equivalent noise energy (ENE) of a single channel for different setups. Larger crystals exhibit higher ENE, primarily due to their lower light yield. Additionally, larger crystals have a broader dynamic range for energy deposition. (b) Energy resolution of a single channel for different setups, incorporating the three digitization processes. Units with smaller crystals achieve better energy resolution.

the formula:

$$ENE = \frac{Noise}{ADC_{p.e.} \times LY_{mea}} \quad (1)$$

where $Noise$ is the number of ADC channels corresponding to electronic noise. For crystals of different sizes, the $Noise$ was set to a constant value of three ADC. $ADC_{p.e.}$ is the number of ADC channels per photoelectron, which varies with gain. LY_{mea} is the light yield measured by SiPM, similar with the values in Figure 9(a). Parameters of $Noise$ and $ADC_{p.e.}$ for one specific setup have already been shown in Table 2, while LY_{mea} is equivalent to the parameter $Lightyield(measured)$ in Table 1. Thus, during the digitization process, different crystal sizes have varying parameters.

As a result, in Figure 10(a), crystals of different sizes exhibit varying ENE values due to differences in light yields. Crystals with higher light yields have smaller ENE. For crys-

tals of the same size, there are three distinct regions in the ENE corresponding to different gain modes. At the transition points between these ranges, the ENE exhibits jumps. Additionally, the dynamic range of energy deposition varies for different configurations. To ensure a balance between maintaining measurement integrity and achieving high measurement precision, we set different ADC dynamic ranges for each configuration, according to the product of the light yield and the maximum deposit energy. After incorporating the three digitization effects in III A 2, the single-channel energy resolution for these configurations is shown in Figure 10(b). Generally, the single-channel energy resolution improves as the crystal size decreases. The transition point around 500 MeV is due to the ENE jump caused by the range switching.

As a result, in Figure 10(a), crystals of different sizes exhibit varying ENE values due to differences in light yields. Crystals with higher light yields have smaller ENE. For crystals of the same size, there are three distinct regions in the ENE corresponding to different gain modes. At the transition points between these ranges, the ENE exhibits jumps. Additionally, the dynamic range of energy deposition varies for different configurations. To ensure a balance between maintaining measurement integrity and achieving high measurement precision, different ADC dynamic ranges were set for each configuration, based on the product of the light yield and the maximum deposited energy. After incorporating the three digitization effects in III A 2, the single-channel energy resolution for these configurations is shown in Figure 10(b). Generally, the single-channel energy resolution improves as the crystal size decreases. The transition point around 500 MeV is due to the ENE jump caused by the range switching.

The performance of the full detector can be determined by applying digitization to each channel. Figure 11(a) and (b) show the energy containment and energy resolution of the ECAL equipped with crystals of different sizes. In these simulations, the overall size of the ECAL was kept around $52 \times 52 \times 48 \text{ cm}^3$. The incident particles are electrons with energies ranging from 1 to 8 GeV, hitting the ECAL's front face within a circular area with a radius of 3 cm at the center. Figure 11(a) shows that if the ECAL is composed of long and thick crystals, its energy containment improves. However, crystal length is more significant than cross-sectional area, as passive material is mainly concentrated in the PCB and copper layers between the layers. For energy resolution, when the ECAL is equipped with crystals of the same cross-sectional area ($2.5 \times 2.5 \text{ cm}^2$) but different lengths, shorter crystals result in better energy resolution. Conversely, when the ECAL is equipped with crystals of the same length (4 cm) but different cross-sectional areas, smaller cross-sectional areas lead to better energy resolution.

Because dark photon signals are often accompanied by significant energy loss in the ECAL, we are more concerned with the low-energy region below 4 GeV. Overall, when the ECAL is equipped with $2.5 \times 2.5 \times 4 \text{ cm}^3$ crystals, it achieves high energy resolution for incident electron energies below 4 GeV while maintaining relatively balanced energy absorption efficiency. Additionally, crystals of this size provide good segmentation, offering potential for multivariate analysis, while

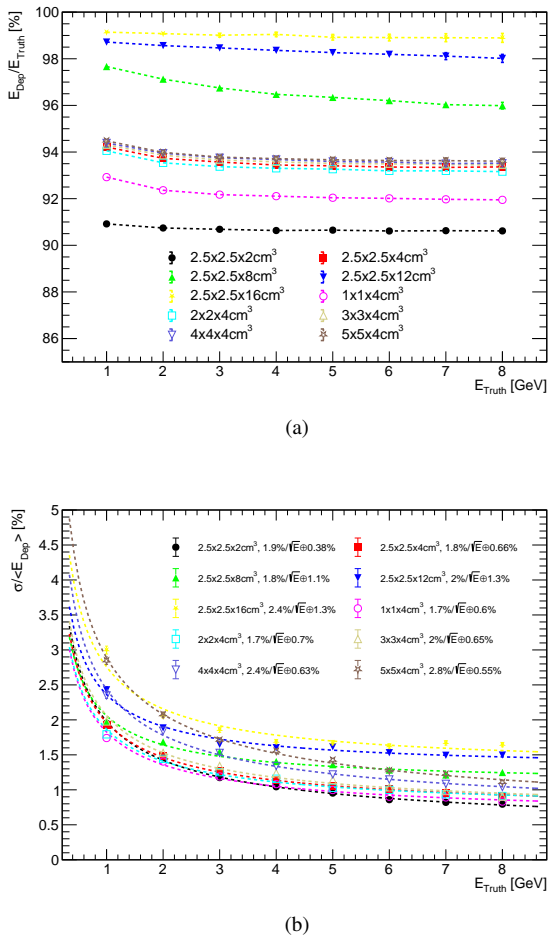


Fig. 11. Energy containment and energy resolution of the ECAL equipped with crystals of different sizes after digitization: (a) Ratio of deposited energy in the ECAL to the truth energy. Smaller crystals in the ECAL introduce a greater amount of passive material, resulting in lower energy containment. (b) Energy resolution, showing that ECALs equipped with small crystals have a better energy resolution below 4 GeV.

keeping the number of channels manageable. Therefore, the crystal size of $2.5 \times 2.5 \times 4 \text{ cm}^3$ is optimal for the DarkSHINE ECAL.

D. Volume optimization

As the mass of dark photons increases, they carry more energy from the incident electron, resulting in a larger recoil angle. Figure 12 illustrates the distribution of recoil angles for particles striking the front surface of the ECAL for both inclusive events and dark photon processes with varying masses. The ECAL's cross-sectional area is $52.5 \times 52.5 \text{ cm}^2$. The majority of inclusive background processes involve electrons directly traversing the target and striking the central region of the ECAL, despite some divergence in the beam spot and slight displacement of electrons due to the magnetic field.

In contrast, signal processes exhibit more dispersed recoil angles. Moreover, with increasing dark photon mass, more events occur in the peripheral region, indicating a higher likelihood of missing the ECAL. These events can be captured and vetoed by the HCAL. Therefore, increasing the ECAL volume can improve signal efficiency, though cost considerations must also be addressed.

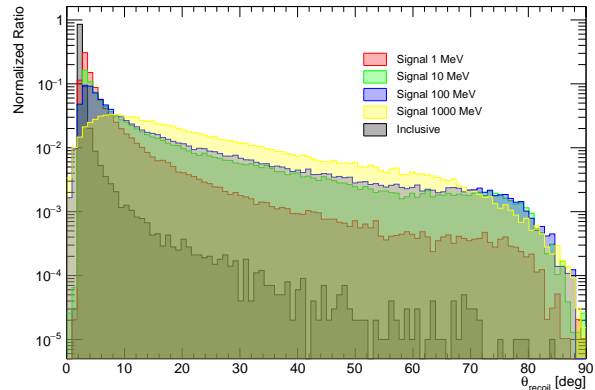


Fig. 12. Dark photon signals exhibit larger recoil angles compared to inclusive background processes. As the mass of the dark photon increases, more events tend to hit on the peripheral regions of the ECAL.

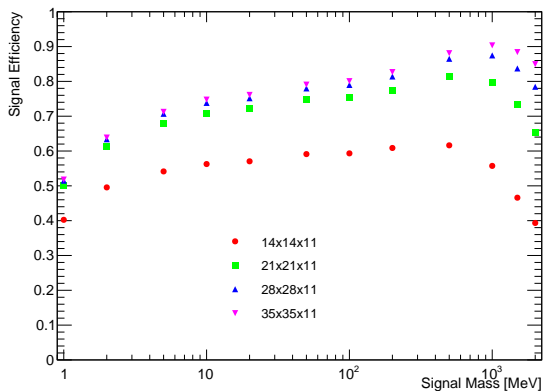
A signal region for the calorimeter is defined as shown in Table 4: the total energy in the ECAL is less than 2.5 GeV, the total energy in the HCAL is less than 30 MeV, and the maximum energy of a single unit in the HCAL is less than 0.1 MeV. This signal region is designed to achieve low background within 3×10^{14} EOTs. It is derived from the combined analysis of all sub-detectors, using thresholds for the ECAL and other sub-detectors, and applying extrapolation methods to exclude all backgrounds[31, 45]. The optimization results of the ECAL are evaluated by the number of events entering the signal region.

Table 4. Signal box for calorimeters.

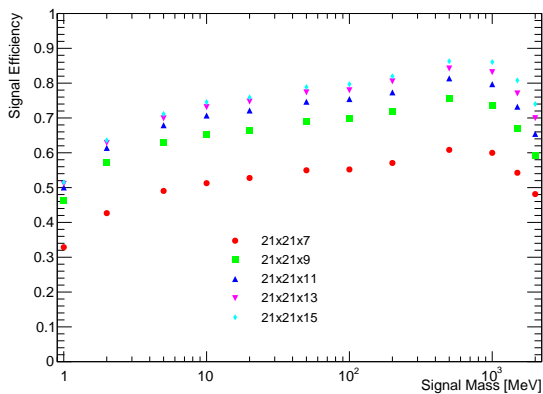
ECAL	HCAL
$E_{ECAL}^{total} < 2.5 \text{ GeV}$	$E_{HCAL}^{total} < 30 \text{ MeV}, E_{HCAL}^{MaxCell} < 0.1 \text{ MeV}$

To maintain consistency with the prospective study[31], we only use the truth energy here instead of the digitized energy. Additionally, the PCB and copper layers are not included in the geometry here and in subsequent analyses.

The ECAL size was optimized in two dimensions: transverse and longitudinal. The individual crystal size remains constant at $2.5 \times 2.5 \times 4 \text{ cm}^3$, as optimized in section III C. First, the ECAL's transverse dimensions were adjusted while keeping the longitudinal length constant at 11 layers. Four different calorimeter sizes were simulated. Results in Figure 13(a) show that as the transverse size increases, signal efficiency for different dark photon masses also increases. The average signal efficiency for all mass points under each size



(a)



(b)

Fig. 13. Signal efficiency as a function of dark photon mass for various ECAL configurations. (a) Optimization of the transverse size of the ECAL, showing signal efficiency for different transverse dimensions. It demonstrates that increasing the ECAL’s transverse size enhances signal efficiency, particularly for higher dark photon masses. (b) Optimization of the longitudinal size of the ECAL, showing signal efficiency for different longitudinal dimensions. It shows that increasing the ECAL’s longitudinal size improves signal efficiency.

is listed in Table 5.

Table 5. Average signal efficiency with varying transverse size of the ECAL.

Number of crystals	Average signal efficiency(%)
14×14×11	53.32
21×21×11	70.78
28×28×11	75.75
35×35×11	77.62

The width of the ECAL was increased by 7 crystal blocks each time. From a design with 14×14×11 crystals to one with 21×21×11 crystals, the ECAL area increased by 2.25 times, resulting in a 17.46% improvement in signal efficiency. However, when the number of crystals per layer reaches

35×35, the increase in signal efficiency becomes marginal. Considering the cost of crystals, an ECAL with 21×21 crystals is deemed appropriate.

Table 6. Average signal efficiency with varying longitudinal size of the ECAL.

Number of crystals	Average signal efficiency(%)
21×21×7	52.05
21×21×9	66.32
21×21×11	71.52
21×21×13	74.07
21×21×15	76.71

The impact of the longitudinal size of the detector on signal efficiency was also investigated. Each time the detector volume was changed, the ECAL’s transverse dimensions were kept constant as 21×21 crystals, and two layers were added longitudinally. Thus, the number of added crystals remained the same each time. Table 6 shows that from the size of 11 layers, the growth in average signal efficiency begins to slow. Therefore, 11 longitudinal layers were chosen as the final size.

Overall, an ECAL size of 52.5×52.5×44 cm³ provides significant signal efficiency while maintaining reasonable cost.

IV. ENERGY DISTRIBUTION

As a fixed target experiment, incident particles without significant energy loss primarily hit the central area of the ECAL, resulting in substantial energy deposition in the central region’s crystals in the first few layers. Additionally, the energy absorbed by crystals in different regions varies greatly, with those closer to the edges typically experiencing minimal energy deposition. To determine the energy dynamic range of the future detector and explore potential triggering methods for the ECAL, the energy deposition in crystals from different regions was investigated.

A. Energy deposition in different regions

With the optimized ECAL configuration in III C and III D, the energy deposition in crystals for dark photon signals and background processes is shown in Figure 14. Inclusive background processes result in larger energy deposition in the crystals, up to 4 GeV. Energy deposition for dark photon signals is slightly lower, with smaller mass dark photons depositing more energy. The dark photon process with a 1 MeV dark photon mass can deposit up to 3.5 GeV of energy in the crystals, as dark photons have a very low probability of carrying minimal kinetic energy, resulting in the recoiling electron retaining most of its energy.

The ECAL was divided into four sections (Figure 15) from the center of the shower to the periphery to study energy deposition in different regions. The number of crystals in each

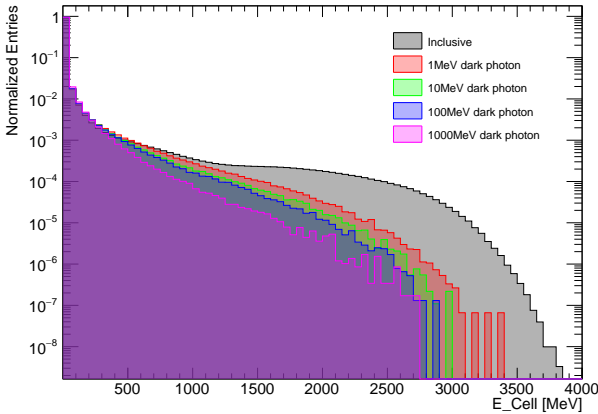


Fig. 14. Energy deposited in single crystals under 8 GeV electron beam. This figure indicates that for inclusive background processes, the energy absorbed by a single crystal can reach up to 4 GeV, while for dark photon signal processes, it can reach up to 3.5 GeV.

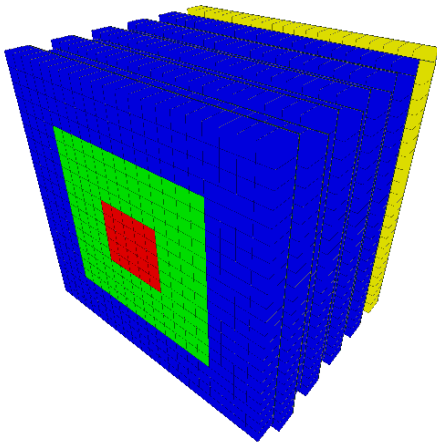


Fig. 15. ECAL divided into four regions, from the center of the shower to the periphery. Red: region-I, green: region-II, blue: region-III, yellow: region-IV.

region is shown in Table 7. Region-I (red) is the core area of shower development, containing 125 crystals each with a volume of $2.5 \times 2.5 \times 4 \text{ cm}^3$, approximately equivalent to 18 radiation lengths. It covers the entire beam spot with a radius of 3 cm and an additional area of one Molière radius. The energy absorbed by each crystal in these four regions is shown in Figure 16. Crystals in the central and near-central regions absorb significantly more energy. In contrast, crystals in Region-III and Region-IV, farther from the shower center, absorb noticeably less energy. For dark photon signals, the energy deposition is even lower than for inclusive background. Figure 17 shows that crystals in Region-I, with only 2.6% of the volume, absorb more than 90% of the energy for inclusive backgrounds.

Table 7. Number of crystals in each region shown in Figure 15

Dimension	Region-I	Region-II	Region-III	Region-IV
x	5	13	21	21
y	5	13	21	21
z	5	7	9	2
Total	125	1058	2786	882

B. Energy limits on crystal

The dynamic range setting affects the accuracy of energy measurement. Generally, a smaller energy dynamic range enables higher measurement accuracy. To determine the minimum dynamic range that meets the energy measurement requirements of the ECAL, an energy limit was applied to each crystal. When the energy deposited in the crystal exceeds these limit values, it is capped at the limit value, simulating the saturation behavior of a real detector. Energy limitations might reduce the total energy measured by the ECAL. Since interest lies in events with significant energy loss, the dynamic range is selected based on the number of events where the total energy measured by the ECAL is less than 4 GeV after applying the energy limits.

Table 8. Ratio of events with total energy less than 4 GeV under different crystal energy limitations.

Energy limit	Inclusive	1 MeV dark photon	10 MeV dark photon
100 MeV	999967/1M	100%	100%
500 MeV	1066/1M	90.57%	96.93%
1000 MeV	3/1M	76.78%	91.23%
2000 MeV	3/1M	76.76%	89.89%
3000 MeV	3/1M	76.76%	89.89%
4000 MeV	3/1M	76.76%	89.89%
6000 MeV	3/1M	76.76%	89.89%
8000 MeV	3/1M	76.76%	89.89%

Energy limit	100 MeV dark photon	1000 MeV dark photon
100 MeV	100%	100%
500 MeV	98.27%	99.5%
1000 MeV	94.52%	98.56%
2000 MeV	93.52%	98.32%
3000 MeV	93.52%	98.32%
4000 MeV	93.52%	98.32%
6000 MeV	93.52%	98.32%
8000 MeV	93.52%	98.32%

Table 8 shows the ratio of events with total energy less than 4 GeV for the background and dark photon signals of different masses after applying various crystal energy limits. For one million background processes, when the energy limit is set to 1 GeV, almost no events pass the cut, except for two photon-muon pair processes and one nuclear process, which can be vetoed by the HCAL. This indicates that very few crystals have an energy deposition exceeding 1 GeV. However, as

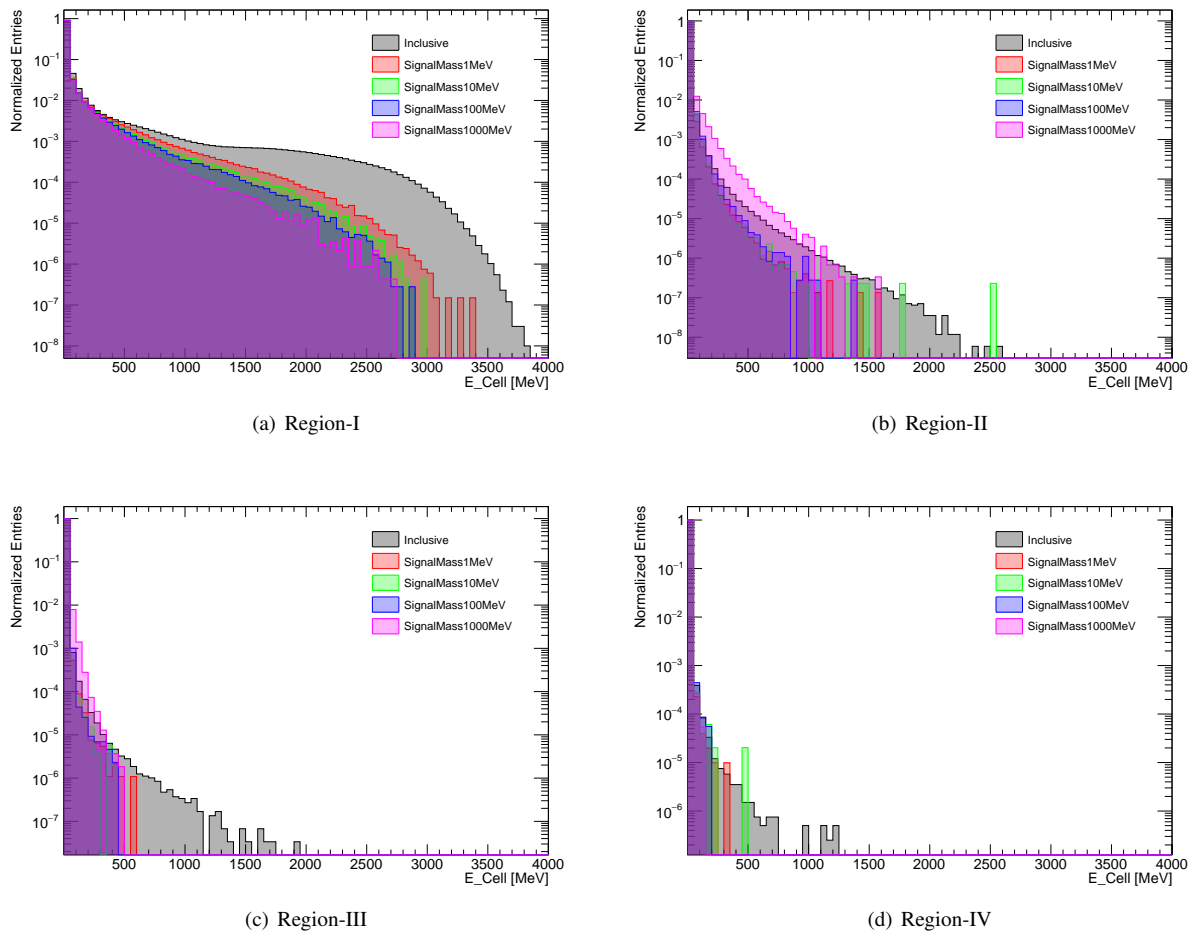


Fig. 16. Energy absorbed by each crystal in the four regions shown in Figure 15. Crystals in the central regions (Region-I and Region-II) absorb significantly more energy, while the crystals in Region-III and Region-IV, farther from the shower center, absorb noticeably less energy.

shown in Figure 18, the total energy measured by the ECAL is significantly lower than the true value at this limit. Additionally, as the number of events increases, there should be a higher probability of background events entering the sensitive range. From Figure 18, a more suitable energy limit appears to be 4 GeV. At this limit, the total energy measured by the ECAL closely matches the true value, and it is difficult for background cases to enter the sensitive range through saturation. Therefore, a single crystal energy dynamic range of 4 GeV is sufficient for the DarkSHINE ECAL. The readout electronics in future detectors can be designed based on this standard.

C. Trigger efficiency

Since the majority of events collected by the ECAL are background processes that are not of interest, data transmission and storage pressure can be alleviated by implementing trigger strategies based on the energy distribution within the ECAL. Using the criterion of energy less than 4 GeV for event

selection, if the sum of the energy in certain crystals exceeds 4 GeV in an event, the event will not be saved. Given that crystals in Region-I absorb most of the energy from the recoiling electron, this region should exhibit the highest trigger efficiency.

Table 9 shows the trigger efficiency with the energy of different regions. By using only 125 crystals in Region-I, more than 99% of the inclusive backgrounds can be filtered out. When using the sum of the energy from all crystals in the ECAL for triggering, an efficiency of nearly 100% can be achieved, except for several rare background processes. For the dark photon signal, this trigger will not cause any impact because the actual signal region requires the total energy in the ECAL to be less than 2.5 GeV.

V. RADIATION DAMAGE

Given the high-energy and high-frequency beam environment, the ECAL, particularly its central region, is subjected to significant radiation doses that may degrade its performance.

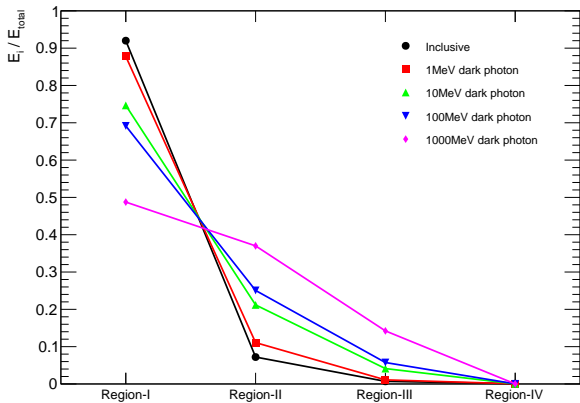


Fig. 17. Energy ratio in different regions for different processes. Both signal and background processes deposit more energy in Region-I. However, for dark photon signal processes, as the dark photon mass increases, more energy is absorbed in the outer regions.

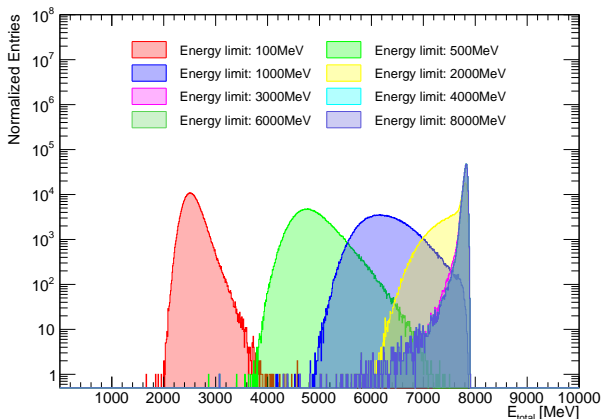


Fig. 18. Energy distribution after applying energy limits on crystals. When the energy limit is too low, background events can enter the signal box. However, when the energy limit reaches 4 GeV, the total energy closely matches the true value.

Therefore, the radiation damage to the ECAL must be evaluated, focusing on crystal damage primarily from ionizing energy loss and silicon sensor damage from non-ionizing energy loss. Simulations were conducted using Geant4 to estimate the radiation damage to crystals and silicon sensors over one year.

Radiation damage to crystals mainly results from ionizing energy loss of incident particles, evaluated by the absorbed dose—the ionizing energy absorbed per unit volume of the crystal. In the simulation, the dose absorbed by each crystal per year of detector operation was recorded. For the crystals receiving the maximum dose, the absorbed dose is about 10^7 rad (Figure 19(a)). Most inorganic scintillators commonly used in high-energy physics detectors, like CsI, BGO, and PWO, lose significant light yield after such a dose. However,

Table 9. Ratio of events with region energy less than 4 GeV.

Trigger region	Inclusive	1 MeV dark photon	10 MeV dark photon
No trigger	1M/1M	100%	100%
I	746/1M	77.57%	91.58%
I+II	37/1M	74.05%	90.03%
I+II+III	6/1M	73.78%	89.9%
I+II+III+IV	3/1M	73.75%	93.57%

Trigger region	100 MeV dark photon	1000 MeV dark photon
No trigger	100%	100%
I	94.86%	98.75%
I+II	93.67%	98.35%
I+II+III	93.57%	98.32%
I+II+III+IV	93.57%	98.32%

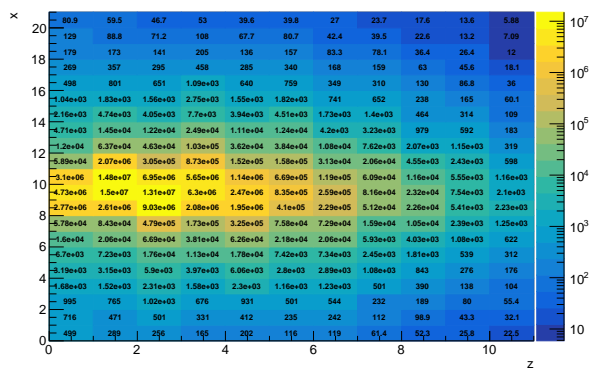
LYSO exhibits only a small reduction in light yield[47], meeting the radiation resistance requirements for the DarkSHINE ECAL. However, ionizing energy loss within the crystal can also lead to uneven response and fluorescent effects, which need more investigation and test.

Radiation damage to silicon sensors mainly results from non-ionizing energy loss, typically expressed using an equivalent 1 MeV neutron fluence. First, the cumulative non-ionizing energy loss E_1 accumulated by each sensor over one year was simulated. Then, the average non-ionizing energy deposition E_2 for 1 MeV neutrons passing through one silicon sensor was calculated. The ratio E_1/E_2 represents the equivalent neutron fluence for one year's operation. In the DarkSHINE ECAL, the equivalent 1 MeV neutron fluence of silicon sensors in the most heavily irradiated area is about 10^{13} (Figure 19(b)). This significant dose could cause the dark current of most commercial silicon sensors to increase by several orders of magnitude, rendering them unusable. Therefore, silicon sensors with excellent radiation resistance are required, as indicated in studies[48–50].

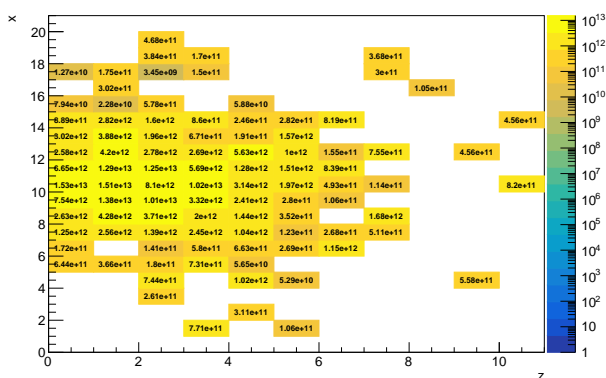
VI. CONCLUSION

This paper details the design and optimization of the LYSO crystal-based electromagnetic calorimeter (ECAL) for the DarkSHINE experiment, aimed at detecting dark photons, potential candidates for dark force mediators. The study involved comprehensive simulations and evaluations to identify an optimal ECAL configuration, balancing performance, cost, and durability.

The chosen crystal size of $2.5 \times 2.5 \times 4$ cm³ emerged from a meticulous analysis of energy containment and resolution for electrons with energies between 1 and 8 GeV. This crystal size ensures high energy resolution and effective energy absorption while maintaining a manageable number of channels for data acquisition. The ECAL's overall dimensions of $52.5 \times 52.5 \times 44$ cm³ were selected to provide a substantial signal efficiency while considering construction and operational costs.



(a)



(b)

Fig. 19. Distribution of radiation damage in ECAL area over one year of operation (a) Radiation dose absorbed by crystals, with a maximum value of 10^7 rad. (b) Equivalent 1 MeV neutron fluence in silicon sensors, with a maximum value of $10^{13} N_{eq}$.

The energy deposition patterns within the ECAL were studied, revealing that crystals near the center absorbed significantly more energy than those at the periphery. This understanding led to the determination of a suitable dynamic range for energy measurements, with a 4 GeV energy limit per crystal found to be adequate. This limit ensures that the ECAL can accurately measure energy deposits while filtering out the majority of background processes. Additionally, potential triggering strategies based on energy distribution were proposed to enhance data processing efficiency.

The radiation tolerance of the ECAL components was also assessed, highlighting the suitability of LYSO crystals due to their small light yield reduction under high radiation doses. The silicon sensors selected for the ECAL should also have excellent resistance to radiation-induced damage, crucial for maintaining detector performance in the high-radiation environment anticipated for the DarkSHINE experiment.

In summary, the ECAL design for DarkSHINE incorporates a robust configuration of LYSO crystals and radiation-resistant silicon sensors, optimized through extensive simulation studies. This design ensures high sensitivity to dark photon signals, efficient background rejection, and reliable performance under challenging conditions. The detailed simulation and optimization efforts have culminated in a matured and robust ECAL design to greatly substantiate the future DarkSHINE experiment.

VII. BIBLIOGRAPHY

- [1] Dan Hooper, Douglas P. Finkbeiner, and Gregory Dobler. Possible evidence for dark matter annihilations from the excess microwave emission around the center of the Galaxy seen by the Wilkinson Microwave Anisotropy Probe. *Phys. Rev. D*, 76:083012, 2007.
- [2] Douglas Clowe, Maruša Bradač, Anthony H. Gonzalez, Maxim Markevitch, Scott W. Randall, Christine Jones, and Dennis Zaritsky. A direct empirical proof of the existence of dark matter*. *The Astrophysical Journal*, 648(2):L109, aug 2006.
- [3] Yong Du, Fei Huang, Hao-Lin Li, Yuan-Zhen Li, and Jiang-Hao Yu. Revisiting dark matter freeze-in and freeze-out through phase-space distribution. *JCAP*, 04(04):012, 2022.
- [4] E. Aprile et al. First Dark Matter Search with Nuclear Recoils from the XENONnT Experiment. *Phys. Rev. Lett.*, 131(4):041003, 2023.
- [5] Yue Meng et al. Dark Matter Search Results from the PandaX-4T Commissioning Run. *Phys. Rev. Lett.*, 127(26):261802, 2021.
- [6] Yi Wang et al. First experimental constraints on wimp couplings in the effective field theory framework from cdex. *Science China Physics, Mechanics & Astronomy*, 64(8), April 2021.
- [7] J. Aalbers et al. First dark matter search results from the lux-zepplin (lz) experiment. *Phys. Rev. Lett.*, 131:041002, Jul 2023.
- [8] F. Giovacchini, J. Casaus, and A. Oliva. The AMS-02 RICH detector: Status and physics results. *Nucl. Instrum. Meth. A*, 952:161797, 2020.
- [9] Dimitrios Kyratzis. Results overview from the DAMPE space mission in orbit. *PoS, PANIC2021:310*, 2022.
- [10] Stefano Giagu. WIMP Dark Matter Searches With the ATLAS Detector at the LHC. *Front. in Phys.*, 7:75, 2019.
- [11] Kim Griest and Marc Kamionkowski. Unitarity Limits on the Mass and Radius of Dark Matter Particles. *Phys. Rev. Lett.*, 64:615, 1990.
- [12] Chiu Man Ho and Robert J. Scherrer. Limits on MeV Dark Matter from the Effective Number of Neutrinos. *Phys. Rev. D*, 87(2):023505, 2013.
- [13] Gary Steigman. Equivalent Neutrinos, Light WIMPs, and the Chimera of Dark Radiation. *Phys. Rev. D*, 87(10):103517, 2013.
- [14] Céline Boehm, Matthew J. Dolan, and Christopher McCabe. A Lower Bound on the Mass of Cold Thermal Dark Matter from Planck. *JCAP*, 08:041, 2013.
- [15] Kenneth M. Nollett and Gary Steigman. BBN And The CMB

- Constrain Light, Electromagnetically Coupled WIMPs. *Phys. Rev. D*, 89(8):083508, 2014.
- [16] Kenneth M. Nollett and Gary Steigman. BBN And The CMB Constrain Neutrino Coupled Light WIMPs. *Phys. Rev. D*, 91(8):083505, 2015.
- [17] Pasquale Dario Serpico and Georg G. Raffelt. MeV-mass dark matter and primordial nucleosynthesis. *Phys. Rev. D*, 70:043526, 2004.
- [18] Julien Billard et al. Direct detection of dark matter—APPEC committee report*. *Rept. Prog. Phys.*, 85(5):056201, 2022.
- [19] Bob Holdom. Two U(1)'s and Epsilon Charge Shifts. *Phys. Lett. B*, 166:196–198, 1986.
- [20] Robert Foot and Xiao-Gang He. Comment on Z Z-prime mixing in extended gauge theories. *Phys. Lett. B*, 267:509–512, 1991.
- [21] Kaori Fuyuto, Xiao-Gang He, Gang Li, and Michael Ramsey-Musolf. cp -violating dark photon interaction. *Phys. Rev. D*, 101:075016, Apr 2020.
- [22] Gongjun Choi, Tsutomu T. Yanagida, and Norimi Yokozaki. A model of interacting dark matter and dark radiation for H_0 and σ_8 tensions. *JHEP*, 01:127, 2021.
- [23] Yu Cheng, Xiao-Gang He, Michael J. Ramsey-Musolf, and Jin Sun. CP violating dark photon kinetic mixing and type-III seesaw model. *Physical Review D*, 105(9), May 2022.
- [24] D. Banerjee et al. Dark matter search in missing energy events with NA64. *Phys. Rev. Lett.*, 123(12):121801, 2019.
- [25] Henso Abreu et al. Search for dark photons with the faser detector at the lhc. *Physics Letters B*, 848:138378, 2024.
- [26] F. Abudinén et al. Search for a dark photon and an invisible dark higgs boson in $\mu^+\mu^-$ and missing energy final states with the belle ii experiment. *Phys. Rev. Lett.*, 130:071804, Feb 2023.
- [27] Yu Zhang, Wei-Tao Zhang, Mao Song, Xue-An Pan, Zhong-Ming Niu, and Gang Li. Probing invisible decay of a dark photon at besiii and a future super tau charm factory via monophoton searches. *Phys. Rev. D*, 100:115016, Dec 2019.
- [28] Vindhyawasini Prasad. Dark matter/ new physics searches at BESIII. *PoS, ALPS2019:030*, 2020.
- [29] Torsten Akesson et al. A high efficiency photon veto for the light dark matter experiment. *Journal of High Energy Physics*, 2020, 04 2020.
- [30] Marco Fabbrichesi, Emidio Gabrielli, and Gaia Lanfranchi. The Dark Photon. 5 2020.
- [31] Jing Chen et al. Prospective study of light dark matter search with a newly proposed DarkSHINE experiment. *Sci. China Phys. Mech. Astron.*, 66(1):211062, 2023.
- [32] S. Li. Dark shine — a dark photon search initiative at shine facility. Jul.
- [33] Jun Wan, Yongbin Leng, Bo Gao, Fangzhou Chen, Jie Chen, Longwei Lai, Weimin Zhou, and Wenzhen Xu. Simulation of wire scanner for high repetition free electron laser facilities. *Nucl. Instrum. Meth. A*, 1026:166200, 2022.
- [34] Zhen-Tang Zhao, Chao Feng, and Kai-Qing Zhang. Two-stage EEHG for coherent hard X-ray generation based on a superconducting linac. *Nucl. Sci. Tech.*, 28(8):117, 2017.
- [35] T. Kimble, M. Chou, and B.H.T. Chai. Scintillation properties of lyso crystals. In *2002 IEEE Nuclear Science Symposium Conference Record*, volume 3, pages 1434–1437 vol.3, 2002.
- [36] Collaboration CMS. A MIP Timing Detector for the CMS Phase-2 Upgrade. Technical report, CERN, Geneva, 2019.
- [37] V. Kalinnikov, E. Velicheva, and A. Rozhdestvensky. Measurement of the LYSO:Ce and LYSO:Ce,Ca Scintillator Response for the Electromagnetic Calorimeter of the COMET Experiment. *Phys. Part. Nucl. Lett.*, 20(5):995–1001, 2023.
- [38] Nicoleta Dinu. 8 - silicon photomultipliers (sipm). In Bahram Nabet, editor, *Photodetectors*, pages 255–294. Woodhead Publishing, 2016.
- [39] Frank Simon. Silicon photomultipliers in particle and nuclear physics. *Nuclear Instruments and Methods in Physics Research Section A: Accelerators, Spectrometers, Detectors and Associated Equipment*, 926:85–100, 2019. Silicon Photomultipliers: Technology, Characterisation and Applications.
- [40] S. Agostinelli et al. GEANT4—a simulation toolkit. *Nucl. Instrum. Meth. A*, 506:250–303, 2003.
- [41] HAHAMATSU S4160-3010PS. https://www.hamamatsu.com.cn/cn/zh-cn/product/optical-sensors/mppc/mppc_mppc-array/S14160-3010PS.html.
- [42] Katsushige Kotera, Weonseok Choi, and Tohru Takeshita. Describing the response of saturated sipms, 2016.
- [43] Claudio Piemonte and Alberto Gola. Overview on the main parameters and technology of modern silicon photomultipliers. *Nuclear Instruments and Methods in Physics Research Section A: Accelerators, Spectrometers, Detectors and Associated Equipment*, 926:2–15, 2019. Silicon Photomultipliers: Technology, Characterisation and Applications.
- [44] Ferenc Nagy, Massimo Mazzillo, Lucio Renna, Giuseppina Valvo, Delfo Sanfilippo, Beatrice Carbone, Angelo Piana, Giorgio Fallica, and József Molnár. Afterpulse and delayed crosstalk analysis on a stmicroelectronics silicon photomultiplier. *Nuclear Instruments and Methods in Physics Research Section A: Accelerators, Spectrometers, Detectors and Associated Equipment*, 759:44–49, 2014.
- [45] Zhen Wang et al. A design of hadronic calorimeter for dark-shine experiment, 2024.
- [46] Eder Izaguirre, Gordan Krnjaic, Philip Schuster, and Natalia Toro. Testing GeV-Scale Dark Matter with Fixed-Target Missing Momentum Experiments. *Phys. Rev. D*, 91(9):094026, 2015.
- [47] Ren-Yuan Zhu et al. Ultrafast and Radiation Hard Inorganic Scintillators for Future HEP Experiments. *J. Phys. Conf. Ser.*, 1162(1):012022, 2019.
- [48] Alexei Ulyanov, David Murphy, Joseph Mangan, Viyas Gupta, Wojciech Hajdas, Daithi De Faoite, Brian Shortt, Lorraine Hanlon, and Sheila McBreen. Radiation Damage Study of SensL J-Series Silicon Photomultipliers Using 101.4 MeV Protons. 7 2020.
- [49] S. Sanchez Majos et al. Noise and radiation damage in silicon photomultipliers exposed to electromagnetic and hadronic radiation. *Nucl. Instrum. Meth. A*, 602:506–510, 2009.
- [50] Roberto Preghenella et al. A sipm-based optical readout system for the eic dual-radiator rich. *Nuclear Instruments and Methods in Physics Research Section A: Accelerators, Spectrometers, Detectors and Associated Equipment*, 1046:167661, 2023.